Nanomotor mechanisms and motive force distributions from nanorotor trajectories

Amir Nourhani,[1,2] Young-Moo Byun,[1] Paul E. Lammert,[1] Ali Borhan,[2,*] and Vincent H. Crespi[1,3,4,†]
[1]*Department of Physics, Pennsylvania State University, University Park, Pennsylvania 16802, USA*
[2]*Department of Chemical Engineering, Pennsylvania State University, University Park, Pennsylvania 16802, USA*
[3]*Department of Chemistry, Pennsylvania State University, University Park, Pennsylvania 16802, USA*
[4]*Department of Materials Science and Engineering, Pennsylvania State University, University Park, Pennsylvania 16802, USA*
(Received 27 May 2013; revised manuscript received 3 October 2013; published 30 December 2013)

Nanomotors convert chemical energy into mechanical motion. For a given motor type, the underlying chemical reaction that enables motility is typically well known, but the detailed, quantitative mechanism by which this reaction breaks symmetry and converts chemical energy to mechanical motion is often less clear, since it is difficult experimentally to measure important parameters such as the spatial distribution of chemical species around the nanorotor during operation. Without this information on how motor geometry affects motor function, it is difficult to control and optimize nanomotor behavior. Here we demonstrate how one easily observable characteristic of nanomotor operation—the visible trajectory of a nanorotor—can provide quantitative information about the role of asymmetry in nanomotor operation, as well as insights into the spatial distribution of motive force along the surface of the nanomotor, the motive torques, and the effective diffusional motion.

DOI: 10.1103/PhysRevE.88.062317 PACS number(s): 82.70.Dd, 47.63.mf, 05.40.−a

I. INTRODUCTION

Chemically powered self-propelled nanomotors have emerged in the past decade as a new field of nonequilibrium colloid science [1–16], with diverse forms of autonomous [17–28] and nonautonomous (i.e., externally driven) motion [29–33], including cargo-carrying [34–36] and externally controlled motors [37–39]. Although great progress has been achieved in developing new nanomotor mechanisms and functions, the direct measurement of the distribution of motive force across motor surfaces has remained a challenge. Linear nanomotors typically move in relatively unstructured random walks governed by axial propulsion plus orientational diffusion. Nano*rotors* engage in more structured cyclic motion. For nanorotors, the combination of linear velocity, angular velocity, and the alignment of the motor axis to the trajectory—all easily obtained from visible trajectories—suffice to pin down both the motive force and torque, and also provide important clues about the distribution of the force across the surface of the motor, as we describe in this paper. This information, combined with an analysis of stochastic contributions to the motion [40–45], can be useful for nanomotor design and optimization.

To date, most modeling efforts on nanomotors have focused on clarifying the mechanisms of linear motion in axisymmetric nanomotors [46–53]. Axisymmetric linear nanomotors are characterized by a deterministic linear speed v and a stochastic orientational diffusion coefficient D_o (plus a trivial contribution from translational diffusion D_t which does not couple directly to the powered motion). Therefore, a linear motor has two characteristic times: the time scale for powered motion to overcome translational diffusion, D_t/v^2, and the time scale over which the motor orientation is forgotten, $\tau_o = D_o^{-1}$. Since linear nanomotors are axisymmetric, the motor's symmetry axis is always aligned with the instantaneous propulsive velocity.

In contrast to linear nanomotors, the emerging class of colloidal *rotary* motors remains largely unexplored theoretically. For a nanorotor moving near a flat surface, the combination of rotor plus surface must have a chirality to support rotation. Beyond this simple geometrical fact, some particular mechanisms have been proposed for the origin of the resultant torques, using either electrokinetic or bubble-derived forces which are presumed to be directed either through the rotor's geometrical center in various directions or off axis, as depicted in Fig. 1 [17–20]. Rotary motors introduce a new time scale $\tau_\omega = \omega^{-1}$ set by the magnitude ω of the angular velocity $\boldsymbol{\omega} = \omega\hat{\omega}$, where $\hat{\omega}$ is a unit vector perpendicular to the substrate and pointing into or away from it according to the chirality (clockwise or counterclockwise, respectively) of

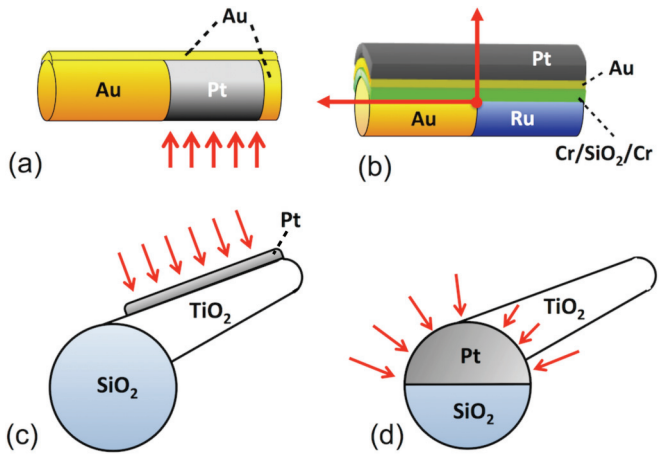

FIG. 1. (Color online) Nanorotors must break axial symmetry in some manner. Experimental implementations include (a) Au/Pt/Au rods with Au cap layer applied to one side [17], (b) Ru/Au rods with insulating Cr/SiO_2/Cr and conductive Au/Pt layers applied to one side [18], (c) tadpole-like SiO_2/TiO_2/Pt structure [19], and (d) tadpole-like SiO_2/Pt/TiO_2 structure [20]. For each motor type, we also reproduce (with red (gray) arrows) the distribution of motive force that was proposed in the original paper.

*borhan@psu.edu
†vhc2@psu.edu

 ©2013 American Physical Society

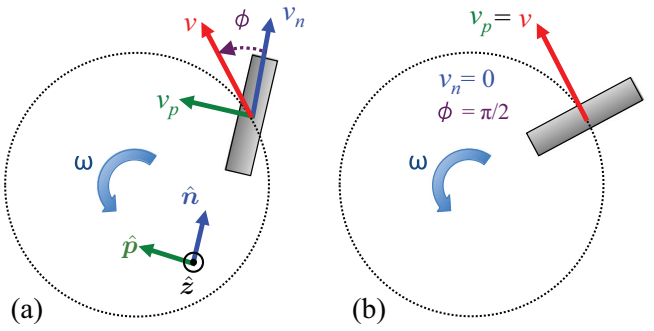

FIG. 2. (Color online) (a) The deterministic motion of a nanorotor along a circular path with some fixed offset ϕ between the nanorotor symmetry axis $\hat{n}$ and the instantaneous velocity $\boldsymbol{v}$. (b) When the velocity along the axis of nanorotor is zero ($v_n = 0$) the nanorod axis is perpendicular to the circular trajectory ($\phi = \pi/2$).

the nanorotor. In contrast to the perfect alignment of propulsion and symmetry axis in an axisymmetric linear nanomotor, the nanorotor's orientation has a nontrivial relationship to the instantaneous direction of its velocity. This relationship can be exploited to extract information about the driving forces along the surface of the rotor.

II. DETERMINISTIC DYNAMICS

Most nanorotors developed to date are based on a cylindrical geometry, with symmetry breaking added through a compositional variation. Hence, they retain a well-defined structural axis which is easily identified in optical microscopy. The asymmetric force distribution acting on a nanorotor generates not only a net torque but also net forces along and perpendicular to this axis. The structural axis of a nanorotor is not necessarily tangent to its trajectory. We define ϕ as the angle between the structural symmetry axis of the nanorod $\hat{n}$ and the translational velocity $\boldsymbol{v}$, as shown in Fig. 2. We choose the direction of the unit vector $\hat{n}$ such that $\hat{n} \cdot \boldsymbol{v} \geqslant 0$. Defining $\hat{p} = \hat{\omega} \times \hat{n}$ as the unit vector perpendicular to the structural symmetry axis $\hat{n}$ and the axis of rotation $\hat{\omega}$, the tuple $(\hat{n}, \hat{p}, \hat{\omega})$ defines a right-handed coordinate system for the body frame of the nanorotor. The angle ϕ can be written in terms of the components of velocity $\boldsymbol{v} = v_n \hat{n} + v_p \hat{p}$ as simply

$$\tan\phi = \frac{v_p}{v_n}. \tag{1}$$

This angle is easily extracted from experimental trajectories. For positive (negative) v_p, the head of the nanorotor points outward (inward) relative to the circular trajectory. Accordingly, ϕ and v_p have the same sign.

Upon selecting a fiducial point $\mathcal{O}$ fixed in the motor's body frame (but not necessarily inside the motor), the instantaneous state of motion decomposes into translational velocity $\boldsymbol{v}$ of $\mathcal{O}$ and rotation of the motor about $\mathcal{O}$ with angular speed ω which is independent of $\mathcal{O}$. On symmetry grounds, the ideal (i.e., purely deterministic) trajectory of a nanorotor must be circular. The boundary integral fluid dynamics simulations of tadpole-like nanotrotors near a surface by Gibbs *et al.* [20] show such a circular path. The radius of the circular trajectory followed by $\mathcal{O}$ is then

$$R = \frac{\sqrt{v_n^2 + v_p^2}}{\omega} \equiv \frac{v}{\omega}. \tag{2}$$

Stochastic orientational dynamics will distort the deterministic circular trajectory to the quasicircular path that we observe in actual experimental nanorotors; we discuss the interplay of deterministic and stochastic motion later.

Using the observed velocity and angular speed of the rotor to gain insight into the motor mechanism requires a clear understanding of how the motive force and torque are expressed in the motion. The *net* force (torque) on the rotor, being the sum of *motive* forces (torques) and *drag* forces (torques), is at all times very nearly zero. One particular way of splitting up the forces (torques) commends itself, as we now explain by exploiting two thought experiments for a given nanorotor geometry. Suppose, as thought experiment 1, that an operating nanorotor is held immobile by external force $-\boldsymbol{F}$ and $\hat{\omega}$ component of torque $-L_{\hat{\omega}}$ about $\mathcal{O}$, the combination being denoted as $[-\boldsymbol{F}, -L_{\hat{\omega}}(\mathcal{O})]$. Notionally, with a finely controlled magnetic field, this could be done by means of a permanent magnet embedded in the rotor. The *motive* force and torque about $\mathcal{O}$ are then by definition $\boldsymbol{F}$ and $L_{\hat{\omega}}$, precisely the force and torque the external agent counters. These may very well include viscous drag forces which a designer would regard as undesirable side effects and not part of the mechanism.

In thought experiment 2, the external force and torque combination $[\boldsymbol{F}, L_{\hat{\omega}}(\mathcal{O})]$ is applied to a nonfunctioning rotor (i.e., no fuel around the rotor). Since fluid dynamics around the nanorotor is in the low-Reynolds-number Stokes-flow regime, the steady state motion $(\boldsymbol{v}, \omega)$ is linearly related to the applied $[\boldsymbol{F}, L_{\hat{\omega}}(\mathcal{O})]$ [54,55]:

$$\begin{pmatrix} \boldsymbol{F} \\ L_{\hat{\omega}} \end{pmatrix} = \left(\begin{array}{c|c} \mathbb{A} & \boldsymbol{B} \\ \hline \boldsymbol{B}^T & d_{\hat{\omega}} \end{array}\right) \begin{pmatrix} \boldsymbol{v} \\ \omega \end{pmatrix}. \tag{3}$$

The symmetric tensor $\mathbb{A}$ and vector $\boldsymbol{B}$ are constant in the body frame, and along with the scalar $d_{\hat{\omega}}$ depend only on the shape of the motor and the location of $\mathcal{O}$.

In a *linear regime* it is legitimate to superpose thought experiments 1 and 2, that is, add together the fluid velocity fields, external forces (which cancel), ion currents, body forces, etc., to obtain the actual conditions of motor operation. The motive $[\boldsymbol{F}, L_{\hat{\omega}}(\mathcal{O})]$ can therefore be deduced from the motion given the Stokes resistance characteristics $(\mathbb{A}, \boldsymbol{B}, d_{\hat{\omega}})$, even though the flow pattern driven directly by the motor mechanism may be very different from that around a body simply dragged through the fluid (thought experiment 2). Low Reynolds number is the rule for nanomotors, so the practical requirement for linearity to be valid (allowing the thought experiment superposition) is that the fluid flow does not appreciably perturb the transport processes directly involved in the motor mechanism. For instance, for an electrokinetic motor moving with speed $v \sim 10\ \mu$m/s, the relevant transport is that of ions with diffusivity $D \sim 10^3\ \mu\text{m}^2/s$ over distances comparable to the motor size $\ell \sim 1\ \mu$m. With a Péclet number $Pe = v\ell/D \sim 10^{-2}$, diffusion easily dominates advection and the assumption of linearity is good.

A. Analytical treatment

We now make use of the analysis above, plus symmetry principles, to convert Eqs. (3) to a form that can be directly applied to experimentally observable trajectories. If the motor has a mirror symmetry plane containing the vertical line through $\mathcal{O}$, then $\boldsymbol{B}$ has zero component perpendicular to the plane. This follows from considering the situation reflected through that plane: ω and the component of $\boldsymbol{F}$ perpendicular to the plane are reversed, but $\boldsymbol{B}$ must be the same because the shape of the motor is unchanged. If there are two distinct vertical mirror planes through $\mathcal{O}$, then $\boldsymbol{B} = 0$. This situation holds for flattened cylinders or rectangular prisms if $\mathcal{O}$ is the center. However, symmetry is not a necessary condition for $\boldsymbol{B}$ to vanish since it depends on $\mathcal{O}$. There is always a choice of $\mathcal{O}$ which will give $\boldsymbol{B} = 0$ and decouple the $\boldsymbol{F} \leftrightarrow \boldsymbol{v}$ problem from the $L_{\hat{\omega}} \leftrightarrow \omega$ problem. (Note: decoupling is not necessarily possible in three dimensions.) If the motor is almost symmetric, the correct choice will be a point about which the motor is nearly symmetric. Therefore, the relation set (3) can be simplified to

$$\boldsymbol{v} = \mathbb{A}^{-1} \cdot \boldsymbol{F} = \frac{F_n}{a_n}\,\hat{n} + \frac{F_p}{a_p}\,\hat{p}, \tag{4a}$$

$$\omega = \frac{L_{\hat{\omega}}}{d_{\hat{\omega}}}, \tag{4b}$$

and the radius of the circular trajectory (2) becomes

$$R = \frac{\sqrt{(F_n/a_n)^2 + (F_p/a_p)^2}}{L_{\hat{\omega}}/d_{\hat{\omega}}}, \tag{5}$$

where F_n and F_p are the components of the net force in the directions $\hat{n}$ and $\hat{p}$, respectively, and the parameters a_n, a_p, and $d_{\hat{\omega}}$ are numerical coefficients whose values depend on the geometry of the nanorotor and its surroundings.

These equations relate the force and torque produced by the motor to the resulting angular and linear velocity, in terms of well-defined geometrical coefficients. For example, a sphere of radius a (with $\mathcal{O}$ at its center) in an unbounded fluid of viscosity η has $a_n = a_p = 6\pi\eta a$ and $d_{\hat{\omega}} = 8\pi\eta a^3$. ("Unbounded" means a motor embedded in an infinite fluid, with no nearby solid surfaces.) A prolate spheroid of semimajor axis a and semiminor axis b [defined by $a^{-2}x^2 + b^{-2}(y^2 + z^2) = 1$ where $a \geqslant b$] provides a better approximation to the shape of actual nanorotors: By changing the eccentricity $e = \sqrt{1 - (b/a)^2}$, it can be smoothly transitioned from a sphere to a long thin rod. In an unbounded Stokes flow, the prolate spheroid has shape parameters [55]

$$\begin{aligned} a_n &= (6\pi\eta a)\,\frac{8}{3}e^3\left[-2e + (e^2+1)\ln\left(\frac{1+e}{1-e}\right)\right]^{-1}, \\ a_p &= (6\pi\eta a)\,\frac{16}{3}e^3\left[2e + (3e^2-1)\ln\left(\frac{1+e}{1-e}\right)\right]^{-1}, \\ d_{\hat{\omega}} &= (8\pi\eta a^3)\,\frac{\frac{4}{3}e^3(2-e^2)}{\left[-2e + (e^2+1)\ln\left(\frac{1+e}{1-e}\right)\right]}. \end{aligned} \tag{6}$$

For a rigid body moving near a planar surface (as in most actual nanorotor observations), the resistance coefficients will deviate from the values for an unbounded domain [56]. However, the resistance coefficients in an unbounded domain seem to be reasonable approximations for analyzing the dynamics of nanorotors [19,21].

Video of rod-shaped nanorotors provides $\boldsymbol{v}$, ω, ϕ, and motor dimensions. By approximating a nanorod by a spheroid, the eccentricity e can be assigned based on the length and width of the particle. Using Eq. (6) for unbounded flow as a first approximation and taking advantage of the linearity of Eq. (4b) in ω, we can calculate the net torque $L_{\hat{\omega}} = d_{\hat{\omega}}\,\omega$ on the particle. Using the velocity $\boldsymbol{v}$, the angle ϕ, and the eccentricity, the force can also be calculated as

$$F = \sqrt{F_n^2 + F_p^2} = v\sqrt{a_n^2\cos^2\phi + a_p^2\sin^2\phi}. \tag{7}$$

From a design perspective, we would like to engineer the appropriate force and torque on a particle to obtain desired translational and angular velocities (and orientation). Recasting Eq. (1) with the geometrical coefficients yields

$$\frac{F_p}{F_n} = \frac{a_p}{a_n}\tan\phi, \tag{8}$$

which shows that for a given geometry, ϕ measures the relative strength of the motive forces perpendicular to and along the nanorod's symmetry axis. Figure 3 shows this relation for different values of ϕ as a function of the aspect ratio of the rotor, $a/b = 1/\sqrt{1-e^2}$. For a given angle ϕ, the ratio of the perpendicular force to the parallel force increases for more slender nanorotors, especially for those with large ϕ. Figure 4 shows that increasing the aspect ratio at fixed a (i.e., making the rotor thinner) means less force is required to achieve a desired velocity. For a given shape, the minimum required force for a given velocity occurs when the nanomotor axis is tangent to its trajectory ($\phi = 0$). Since the driving forces F_n and F_p presumably both derive from a fixed total capacity for chemical propulsion, nanorotor performance would thus seem to be maximized when $F_p = 0$. However, a complete design analysis must also take into account the need for the overall force distribution across the surface of the nanoparticle to produce the desired torque.

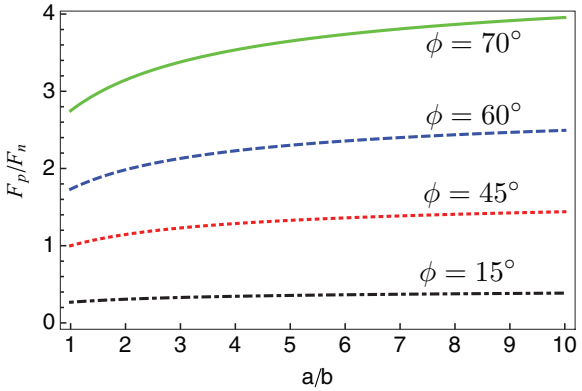

FIG. 3. (Color online) The ratio of the forces perpendicular and parallel to the nanorotor's symmetry axis is largest when the motor is long and slender (i.e., has a large aspect ratio) and is strongly tilted with respect to the motor's direction of motion (i.e., has large ϕ).

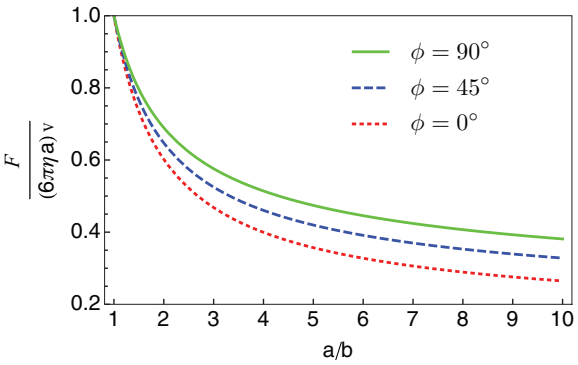

FIG. 4. (Color online) For a given nanorotor shape and magnitude of driving force (at fixed semimajor axis a), the better aligned rotor (i.e., smaller angle ϕ) achieves a larger velocity (the vertical axis plots a dimensionless ratio of driving force to linear velocity). The highest velocity occurs at $\phi = 0$, when the symmetry axis of the spheroidal nanorotor is tangent to the trajectory.

B. Case studies

Having established the basic principles, next we apply them to two practical examples and show how a quantitative analysis of the trajectories can rule out certain propulsive mechanisms and reveal the presence of unanticipated components to the motive force. The cylindrical nanorotor depicted in Fig. 1(a) was posited [17] to operate by a bubble propulsion mechanism exerting forces perpendicular to the axis of the nanorod at the site of the Pt patch, with no force along the axis of the rod (i.e., $F_n = 0$, $F_p \neq 0$). For such a force distribution, the angle in Eq. (8) is $\phi = 90^\circ \equiv \pi/2$, so the axis of the nanorod should point perpendicular to its trajectory, as illustrated in Fig. 2(b). An analysis of the quasicircular path of this nanorotor is demonstrated in Fig. 5. The orientation is actually $\phi \approx -43^\circ$. Thus, the actual force distribution of this nanorotor includes a substantial axial component. For a quantitative analysis, we use the reported dimensions of the rod (length $2a = 5.0$ μm and diameter $2b = 360$ nm) and the angular velocity ($\omega = 2.34$ rad/s) extracted from the video in the supporting information of Ref. [17]. Approximating the rods as prolate spheroids and using Eqs. (6) yields $a_n/(6\pi\eta a) = 0.23$, $a_p/(6\pi\eta a) = 0.35$, and $d_{\hat{\omega}}/(8\pi\eta a^3) = 0.12$. The torque about the center of the rod

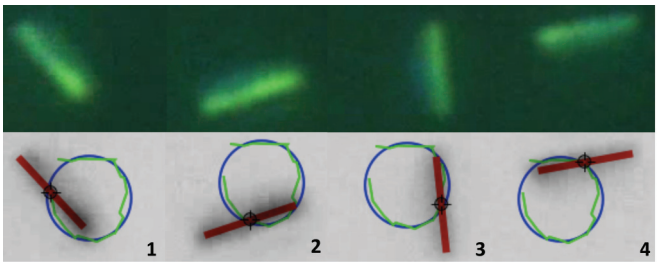

FIG. 5. (Color online) One counterclockwise rotation of the slow nanorotor [17], including the path of the center of mass (green [gray] curve), and a fitted ideal circular trajectory, which omits fluctuations (blue [gray] curve). The rod points slightly inward toward the center of the orbit. The frames are not equally spaced in time. The frames are adapted with permission from the supporting video of Ref. [17]. Copyright (2007) American Chemical Society.

is then $L = d_{\hat{\omega}}\omega = 1.09 \times 10^{-12}$ dyn cm. (Later, we calculate the contribution of angular speed to the torque more precisely from the analysis of rotor trajectory.) From the video analysis, we estimate that the radius of the instantaneous circle is $R \approx 2.2$ μm, so that $\boldsymbol{v} = (3.8\,\hat{n} - 3.6\,\hat{p})$ μm/s (for a rotor, this is likely the best way to find the velocity). Finally, we obtain the motive force $\boldsymbol{F} = (1.6\,\hat{n} - 1.5\,\hat{p}) \times 10^{-8}$ dyn.

As another example, we analyze the motion of in-place-rotating ultrafast nanorotors [18] which are formed by breaking the symmetry of a cylindrical bimetallic Pt/Au nanorod through deposition of a Pt/Au cap on top of an insulating Cr/SiO_2/Cr cap deposited on the side of the Ru/Au cylinder, as depicted in Fig. 1(b). It was conjectured that the Pt/Au cap would pull the nanomotor toward the center of the circular orbit, encouraging it to rotate in place. However, Eq. (5) for the radius of the trajectory's curvature indicates that the addition of a lateral force increases the net force and thus *increases* the radius of the orbit. This leaves open the actual mechanism that facilitates the fast in-place rotation of these particles, including the possibility that the Pt/Au and Au/Ru substructures interact electrically to form a more complex electrochemical geometry.

C. Design principles

In addition to these insights into specific kinds of motors already made, it is also possible to deduce design principles for new motors. One useful design principle is *maximal utilization* of a limited propulsive capacity. Imagine a propulsive mechanism (such as bubble propulsion) which generates a force normal to the surface of the motor. This is a linear constraint on the surface stress. More generally, we can require the surface stress to lie in any linear constraint set $\mathcal{C}$ and find the distribution of force across the motor surface that, for given mean-square traction integrated across the motor surface, $\|\boldsymbol{f}\|^2 = \int |\boldsymbol{f}(\boldsymbol{r})|^2\, dS$, generates the maximum net force $\boldsymbol{F} \cdot \hat{h}$ in a specified direction $\hat{h}$. Thinking in terms of a Hilbert space of vector fields on the surface, we see that the mentioned net force is given by the surface integral $\hat{h} \cdot \boldsymbol{F} = \int \hat{h} \cdot \boldsymbol{f}(\boldsymbol{r})\, dS$, which is the inner product of the vector field $\boldsymbol{f}$ and the constant field equal to $\hat{h}$ at all points on the surface. The maximizing force field is found by orthogonal projection of this field into the constraint space $\mathcal{C}$. The net torque along $\hat{\omega}$ for given $\|\boldsymbol{f}\|$ can be maximized in a similar way, upon noting that $\hat{\omega} \cdot \boldsymbol{L} = \int (\hat{\omega} \times \boldsymbol{r}) \cdot \boldsymbol{f}(\boldsymbol{r})\, dS$ is again given by inner product with a vector field $\hat{\omega} \times \boldsymbol{r}$ which should be projected into $\mathcal{C}$. In general, maximizing one component of the net force is incompatible with maximizing the torque, or with making the orthogonal components of the force zero, but in situations of high symmetry, all can be simultaneously realized. One such case is a prolate spheroid with the previously mentioned constraint that the traction everywhere be normal to the surface. With $\boldsymbol{f}(\boldsymbol{r}) = f(\boldsymbol{r})\hat{n}$, the result in spheroidal coordinates is

$$f(\alpha,\beta) = \frac{F}{4\pi ab}\,(3\cos\beta\,\cos\phi + 4\sin\beta\,\sin\alpha\,\sin\phi) + \frac{L}{4\pi ab(a-b)}\cos\beta\,\sin\beta\,\sin\alpha. \quad (9)$$

The angles α and β are respectively the azimuthal and polar angles on the spheroid (i.e., the analogs of longitude and

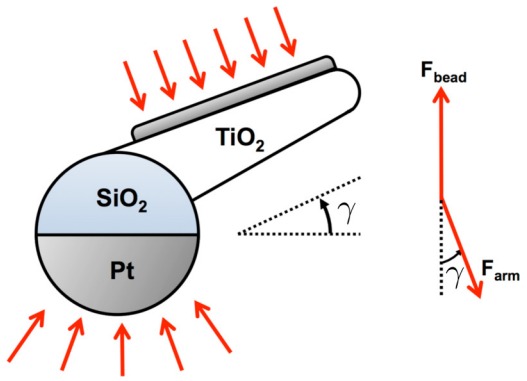

FIG. 6. (Color online) A pair of off-axis opposing forces produces minimal net force and maximal net torque. In this Janus-sphere-plus-arm implementation, as the angle γ of the arm to the sphere's equator becomes smaller, the net force is reduced and the resulting orbit becomes tighter.

lattitude); a and b are the semimajor and semiminor axes of the spheroid. This distribution of force provides the most efficient way to allocate a limited propulsive capacity across the surface of the motor to obtain a desired net force F and net torque L.

The linearity of Stokes flow also can be exploited to design geometries other than cylindrical or spheroidal. Fast in-place rotors require a minimal net force and a maximal net torque; i.e., a center of mass as close as possible to the center of rotation $\mathcal{O}$. The tadpole-like structure shown in Fig. 6 provides one suitable geometry which is compatible with the fabrication methods of references [19] and [57]. The bead is a spherical SiO_2 Janus particle, half-coated with Pt. The top of the TiO_2 arm is also covered by Pt. When the rotor is placed in a hydrogen peroxide solution, the forces on the arm and the lower hemisphere largely cancel, yielding a small net force

$$F_{\text{net}} = \left(F_{\text{arm}}^2 + F_{\text{bead}}^2 - 2F_{\text{arm}}F_{\text{bead}}\cos\gamma\right)^{\frac{1}{2}} \qquad (10)$$

but potentially a large net torque and thus nearly in-place rotation. The length of the arm and angle γ of the arm to the sphere equator can be adjusted to optimize performance, following Eq. (3).

III. STOCHASTIC CONTRIBUTIONS

We have focused so far on the deterministic part of nanorotor dynamics, with perfectly circular orbits. Orientational diffusion complicates this picture. Since the orientational persistence time is $\tau_o = D_o^{-1}$, paths remain close to circular so long as $\tau_\omega \equiv \omega^{-1} \ll \tau_o$, while for $\tau_\omega \gg \tau_o$ the trajectory is nearly indistinguishable from a random walk or a linear nanomotor. In addition to linear velocity and angular speed, we can extract rich information such as orientational diffusion, long-time effective diffusion, the value of $d_{\hat{\omega}}$ and the contribution of ω to the torque in Eq. (3) from relatively short-run videos of nanorotors. We have analyzed trajectories of the slow spinner in Fig. 1(a) (Ref. [17]), the fast rotor in Fig. 1(b) (Ref. [18]), and four tadpole-like rotors with the geometry shown in Fig. 1(d) (Ref. [20]). For all these nanorotors, the fluctuations of the deviation of the rotation angle from the deterministic rotation $\delta\theta(t;\Delta t) = \theta(t+\Delta t) - \theta(t) - \omega\,\Delta t$ for a given time interval Δt is distributed as a nearly zero-mean Gaussian, providing good evidence that these orientational fluctuations are diffusive in nature. Similar behavior has been observed in autonomous runners and tumblers formed from paired Janus particles [42]. We extracted the values of orientational diffusion coefficient D_o from these fluctuations by assuming a standard deviation of the form $\sigma(\Delta t) = \sqrt{2D_o\Delta t}$. For each nanorotor, we calculated $\sigma(\Delta t)$ for a range of values of Δt and fit to the linear relation $[\sigma(\Delta t)]^2 = 2D_o\Delta t$ to extract D_o, as described in Appendix A. The results are shown in Table I (along with results for the contribution of angular speed to torque, obtained as explained below). In all of these cases $\tau_o \gg \tau_\omega$, so the nanorotor follows a close-to-circular trajectory and the deterministic analysis of the motive force and torque given earlier remains a good approximation.

If fluctuations of motor function contribute significantly to diffusion, then the diffusion can tell us something about the motor operation. Such fluctuations should make a contribution to the effective orientational diffusion of about ω^2 divided by the rate of the "events" that drive the motor. Taking an estimated electrochemical event rate of 10^6 s^{-1} for a few-micron-long bimetallic rod moving at a few microns per second as typical, rotational speeds of a few radians per second correspond to a contribution to the total D_o of the order of 10^{-5} rad^2/s, which is negligible compared to the thermal contribution. Thus stochastic fluctuations in an electrochemical propulsive mechanism itself are unlikely to

TABLE I. Nanorotor characteristics calculated on the basis of analysis of published video data, as described in the text. Following Eq. (3), $d_{\hat{\omega}}\omega$ gives the contribution of angular speed to torque. The effective diffusion coefficients D_{eff} are calculated using Eq. (12).

Rotor	ω (rad/s)	v (μm/s)	D_o (rad^2/s)	$d_{\hat{\omega}}$[a] (dyn cm s$\times 10^{13}$)	$d_{\hat{\omega}}\omega$ (dyn cm$\times 10^{12}$)	D_{eff} (μm^2/s)
Slow [17]	2.3	5.2	0.103	3.93	0.90	0.263
Fast [18]	29.3	~30[b]	0.449	0.90	2.64	0.235
tp1 [20][c]	5.6	19.75	0.056	7.23	4.05	0.348
tp2 [20]	3.8	20.09	0.063	6.42	2.44	0.880
tp3 [20]	4.7	14.67	0.046	8.80	4.14	0.224
tp4 [20]	5.3	14.57	0.047	8.61	4.56	0.178

[a]Calculated based on Eq. (11).
[b]Approximated from data in Ref. [58].
[c]tp# stands for tadpole-like nanorotor. Figure (7) shows the numerical identifiers.

contribute significantly to the observed diffusion of a micron-scale motor, due to the rapid pace of such reaction events.

More importantly, thermal diffusion gives us direct access to the Stokes mobility characteristics, automatically including the effect of nearby solid boundaries and not needing any information about the geometry. The connection is a generalization of the familiar Einstein relation and states that the resistance matrix [Eq. (3)] referenced to the center of mass as $\mathcal{O}$ is exactly equal to $k_B T$ times the inverse of the diffusion matrix, where k_B is Boltzmann constant and T is temperature. The general case is discussed in Appendix B. For a cylinder or spheroid, we see that the shape parameter $d_{\hat{\omega}}$ is

$$d_{\hat{\omega}} = \frac{k_B T}{D_o}. \tag{11}$$

Since the $L_{\hat{\omega}} \leftrightarrow \omega$ and $\boldsymbol{F} \leftrightarrow \boldsymbol{v}$ problems are decoupled when $\mathcal{O}$ is the center of mass, this is just the ordinary Einstein relation. For other shapes, such as tadpoles, we can take this as a practical approximation. Applying this technique to our estimate of $D_o^{\text{slow}} = 0.103$ rad^2/s and $\omega = 2.34$ rad/s for the rotor of Ref. [17] yields a torque of 9.0×10^{-13} dyn cm. The very close agreement with our earlier estimate (10.9×10^{-13} dyn cm) obtained from the geometry approximation is probably fortuitous, but it clearly demonstrates the feasibility of this sort of analysis. Table I provides a similar analysis for the other motor types. The contribution of angular speed to torque is of order 10^{-12} dyn cm, and the characteristic time of deterministic rotation τ_ω is much smaller than the orientational persistence time τ_o, i.e., $\tau_\omega/\tau_o = D_o/\omega \sim 10^{-2}$.

Finally, the interplay between the deterministic rotation and stochastic orientational diffusion leads to long-time effective diffusion of the nanorotor with diffusivity [40–44]

$$D_{\text{eff}} = \frac{v^2}{2}\frac{D_o}{D_o^2 + \omega^2}. \tag{12}$$

The observed translational diffusion is the sum of passive diffusion and this effective diffusion. Although one might think that this long-time phenomenon requires lengthy video trajectories to characterize, Eq. (12) shows that it can be derived from knowledge of v, ω, and D_o, all short-time phenomena. Thus we can also provide D_{eff} in Table I. The effective diffusion coefficients are comparable to passive Brownian translational diffusion coefficients ($\sim 10^{-1}$ μm^2/s) of the particles, and the order of magnitude of dimensionless effective diffusivities are $D_{\text{eff}}\,\omega/v^2 \sim 10^{-3}$–$10^{-2}$.

IV. CONCLUDING REMARKS

In summary, nano*rotors* have a richer dynamics than linear nano*motors*, and thus their trajectories provide more information about the microscopic processes that drive their motion. We have shown how these trajectories can be analyzed to draw inferences about the distribution of force and torque about the motor surfaces, and how motor geometry can be engineered to optimize desired behavior, including the orbital radius, the orientation of the motor axis to the trajectory, and the relative role of orientational fluctuations. By analyzing several types of motors in detail, we show how the rotor trajectories provide valuable information about the magnitudes of motives forces and torques, the spatial distributions of motive forces, and the influence of stochastic fluctuations on both short-time and long-time behavior.

ACKNOWLEDGMENT

This work was supported by the NSF under Grant No. DMR-0820404 through the Penn State Center for Nanoscale Science.

APPENDIX A: ANALYZING NANOROTOR VIDEOS

The trajectory of a rotary nanomotor contains rich information about the quantitative aspects of nanorotor dynamics and provides us with quantities such as linear speed v, angular speed ω, orientational diffusivity D_o, and shape coefficient $d_{\hat{\omega}}$. We can then calculate other physical quantities, such as the contribution of angular speed to torque and the long-time effective diffusion coefficient from relatively short videos. Here, we explain how to calculate these related quantities from the videos in the supporting information provided for the slow [17], fast [18], and tadpole-shaped [20] nanorotors.

We analyze the nanorotor trajectory by evaluating the state of the nanorotor (i.e., its position and orientation) in each frame of the video. For a given frame, we transform the relatively high-resolution image into a black and white image with the nanorotor being the only black domain in the image (see Fig. 7). Subsequently, we determine the center of mass of the black pixels for each nanorotor to establish the position of the nanorotor. We also calculate the inertia matrix of the black pixels to find the principal axes, based on which we define the orientation angle θ as that between the horizontal axis and the principal axis with the smaller eigenvalue. The increment (decrement) of the orientation angle θ for counterclockwise (clockwise) rotation is cumulative as we go from one frame to the next, so that the angles are not limited to $[0, 2\pi)$ in a periodic fashion, but increase (decrease) cumulatively. Fitting the orientation angle θ as a function of time t to the linear relation

$$\theta(t) = \omega t + \theta_0 \tag{A1}$$

yields the angular speed ω. The calculated value of ω is indeed an average quantity. The angular fluctuation

$$\Delta\theta(t) = \theta(t) - \omega t \tag{A2}$$

is attributed to stochastic kicks and the resulting orientational diffusion. Figure 8(a) shows the angular fluctuations for the

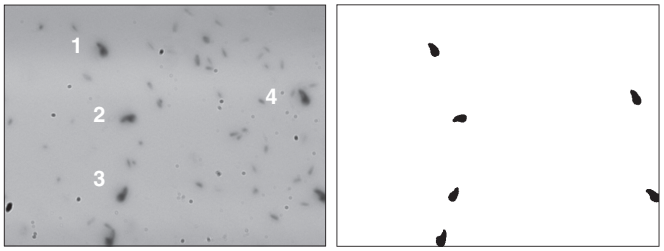

FIG. 7. (Left) Four tadpole-like rotors [20] are picked for analysis. (Right) The frame is converted to black and white for image analysis, where the rotors are black. The frames are adapted with permission from the supporting video of Ref. [20]. Copyright (2011) American Chemical Society.

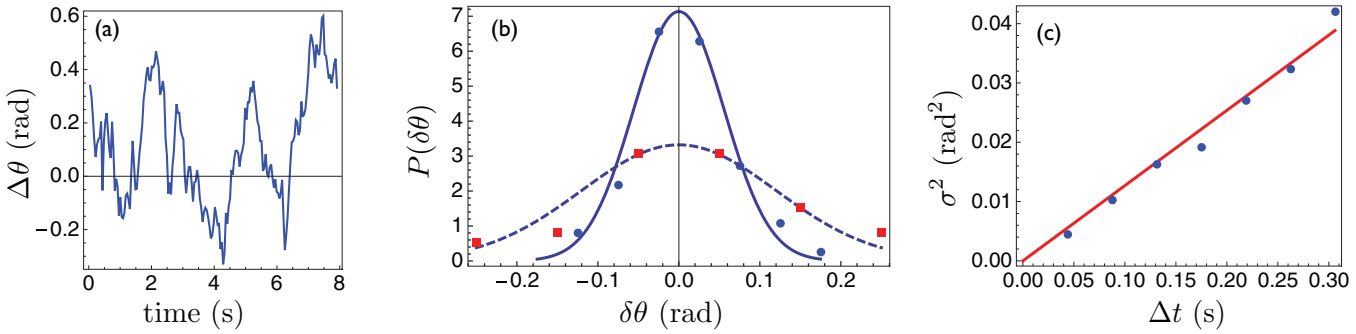

FIG. 8. (Color online) Analysis of tadpole-like nanorotor 2 shown in Fig. (7). (a) Angular fluctuations as a function of time. (b) The distribution of angular fluctuation during a time interval Δt follows a Gaussian distribution at different time intervals Δt. For $\Delta t = 0.044$ s the data (•) fit a Gaussian (solid line) with the standard deviation $\sigma = 0.056$ rad. For larger $\Delta t = 0.131$ s, the Gaussian fit (dashed line) to the data (■) is wider with $\sigma = 0.120$ rad. (c) One half of the slope of the variance σ^2 as a function of Δt gives the orientational diffusion coefficient $D_o = 0.063\,\mathrm{rad}^2/\mathrm{s}$.

portion of video provided in the supporting information of Ref. [20] for the tadpole-like nanorotor 2 identified in Fig. 7. It is clear from the figure that the angular deviation can be significant, showing the effect of the stochastic component on the direction of the nanomotor velocity.

In order to determine the orientational diffusion coefficients from the videos, we calculated the change in the angular fluctuation during the time interval Δt,

$$\delta\theta(t;\Delta t) = \Delta\theta(t+\Delta t) - \Delta\theta(t), \tag{A3}$$

and found the distribution of $\delta\theta(t;\Delta t)$. It is clear from Fig. 8(b) that the distributions follow a zero-mean normal distribution

$$\mathcal{N}(\delta\theta;\langle\delta\theta\rangle = 0,\sigma) = \frac{1}{\sqrt{2\pi\sigma^2}}\exp\left(-\frac{(\delta\theta)^2}{2\sigma^2}\right). \tag{A4}$$

The same behavior is observed for other tadpole-shaped rotors and slow [17] and fast [18] nanorotors. The width of the distribution σ is related to the orientational diffusion coefficient D_o through

$$\sigma^2 = 2D_o\Delta t. \tag{A5}$$

Fitting the data to this expression gives the orientational diffusion coefficient D_o [see Fig. 8(c)], from which we can obtain the shape coefficient $d_{\hat{\omega}}$ using Eq. (11). The results for the slow [17], the fast [18], and four tadpole-like nanorotors [20] are shown in Table I.

APPENDIX B: FLUCTUATION-DISSIPATION RELATION AND THE MOBILITY MATRIX

The famous Einstein relation $D = k_B T\,\mu$ relates the diffusion coefficient D and the mobility μ of a particle, apparently in the case when both of these are scalar quantities, as for a sphere. Here we examine how the relation applies in the more complicated situation of an asymmetric particle with nonisotropic diffusion coupled to orientational diffusion. We start with equations of motion in the form

$$\frac{d\mathcal{P}}{dt} = -\Gamma\mathcal{P} + \mathcal{F}. \tag{B1}$$

Here, $\mathcal{P}$ denotes several momentum-type variables. We have in mind the collection of linear and angular momenta of a rigid particle, though this problem may be of interest in other contexts. Γ is a damping matrix and $\mathcal{F}$ represents external forces and torques (including thermal ones). We will not need to explicitly discuss these, since $\mathcal{F}$ serves only to help us identify the mobility. By means of a mass matrix $\mathcal{M}$ we convert Eq. (B1) to a system of equations for velocity-type variables $\mathcal{V}$ (such as linear and angular velocities) of the form

$$\mathcal{P} = \mathcal{M}\mathcal{V} \tag{B2}$$

to obtain

$$\frac{d\mathcal{V}}{dt} = -\tilde{\Gamma}\mathcal{V} + \mathcal{M}^{-1}\mathcal{F} \tag{B3}$$

with

$$\tilde{\Gamma} = \mathcal{M}^{-1}\Gamma\mathcal{M}. \tag{B4}$$

Thus the mobility is

$$\mu = \tilde{\Gamma}^{-1}\mathcal{M}^{-1} = \mathcal{M}^{-1}\Gamma^{-1}. \tag{B5}$$

Meanwhile, the energy is a quadratic form in the momenta or velocities:

$$E = \mathcal{P}^T\frac{\mathcal{Q}}{2}\mathcal{P} = \mathcal{V}^T\frac{\tilde{\mathcal{Q}}}{2}\mathcal{V}, \tag{B6}$$

with

$$\tilde{\mathcal{Q}} = \mathcal{M}^T\mathcal{Q}\mathcal{M}, \tag{B7}$$

which gives us an equilibrium expectation of

$$\langle\mathcal{V}\otimes\mathcal{V}\rangle = (k_B T)\,\tilde{\mathcal{Q}}^{-1}. \tag{B8}$$

where $\otimes$ is the dyadic product. Combining this with Eq. (B4) with no systematic forcing leads to the autocorrelation

$$\langle\mathcal{V}(t)\otimes\mathcal{V}(0)\rangle = (k_B T)\,e^{-\tilde{\Gamma}t}\,\tilde{\mathcal{Q}}^{-1}. \tag{B9}$$

The final ingredient is a Green-Kubo expression for the diffusion matrix:

$$\mathcal{D} = \int_0^\infty \langle\mathcal{V}(t)\otimes\mathcal{V}(0)\rangle\,dt = (k_B T)\,\tilde{\Gamma}^{-1}\tilde{\mathcal{Q}}^{-1}. \tag{B10}$$

Therefore the mobility in Eq. (B5) can be determined from the diffusion matrix according to

$$\mu = \tilde{\Gamma}^{-1}\mathcal{M}^{-1} = \frac{1}{k_B T}\mathcal{D}\mathcal{M}^T\mathcal{Q}. \tag{B11}$$

If our fiducial point is the center of mass, then it is easy to see that $\mathcal{M}$ is diagonal and $\mathcal{Q} = \mathcal{M}^{-1}$. In that case

$$\mu_{\text{CM}} = \frac{1}{k_B T}\mathcal{D}_{\text{CM}}. \tag{B12}$$

If the random translational and orientational motions are independent, μ is block diagonal and inversion yields Eq. (11); to the extent that rotational-translational coupling is small, that relation remains approximately valid. It is remarkable that we can obtain the angular velocity response to a torque just by observing the orientational diffusion, even if the orientational and translational diffusion are coupled, as is generally the case for an asymmetrical particle.

[1] W. F. Paxton, A. Sen, and T. E. Mallouk, Chem. Eur. J. **11**, 6462 (2005).
[2] S. J. Ebbens and J. R. Howse, Soft Matter **6**, 726 (2010).
[3] T. Mirkovic, N. S. Zacharia, G. D. Scholes, and G. A. Ozin, ACS Nano. **4**, 1782 (2010).
[4] W. F. Paxton, S. Sundararajan, T. E. Mallouk, and A. Sen, Angew. Chem. Int. Ed. **45**, 5420 (2006).
[5] H. H. Kung and M. C. Kung, Appl. Catal. A **309**, 159 (2006).
[6] G. A. Ozin, I. Manners, S. Fournier-Bidoz, and A. Arsenault, Adv. Mater. **17**, 3011 (2005).
[7] J. Wang, ACS Nano. **3**, 4 (2009).
[8] J. Wang, Lab. Chip **12**, 1944 (2012).
[9] D. Kagan, M. J. Benchimol, J. C. Claussen, E. Chuluun-Erdene, S. Esener, and J. Wang, Angew. Chem. Int. Ed. **51**, 7519 (2012).
[10] T. Mirkovic, N. S. Zacharia, G. D. Scholes, and G. A. Ozin, Small **6**, 159 (2010).
[11] G. A. Ozin, ChemCatChem **5**, 2798 (2013).
[12] J. Wang and K. M. Manesh, Small **6**, 338 (2010).
[13] S. Sengupta, M. E. Ibele, and A. Sen, Angew. Chem. Int. Ed. **51**, 8434 (2012).
[14] W. Wang, W. Duan, S. Ahmed, T. E. Mallouk, and A. Sen, Nano Today **8**, 531 (2013).
[15] W. Wang, W. Duan, A. Sen, and T. E. Mallouk, Proc. Natl. Acad. Sci. U.S.A. **110**, 17744 (2013).
[16] W. Wang, T.-Y. Chiang, D. Velegol, and T. E. Mallouk, J. Am. Chem. Soc. **135**, 10557 (2013).
[17] L. Qin, M. J. Banholzer, X. Xu, L. Huang, and C. A. Mirkin, J. Am. Chem. Soc. **129**, 14870 (2007).
[18] Y. Wang, S.-T. Fei, Y.-M. Byun, P. E. Lammert, V. H. Crespi, A. Sen, and T. E. Mallouk, J. Am. Chem. Soc. **131**, 9926 (2009).
[19] J. G. Gibbs and Y.-P. Zhao, Small **5**, 2304 (2009).
[20] J. G. Gibbs, S. Kothari, D. Saintillan, and Y.-P. Zhao, Nano Lett. **11**, 2543 (2011).
[21] J. G. Gibbs and Y.-P. Zhao, Small **6**, 1656 (2010).
[22] S. Fournier-Bidoz, A. C. Arsenault, I. Manners, and G. A. Ozin, Chem. Commun. 441 (2005).
[23] Z. Fattah, G. Loget, V. Lapeyre, P. Garrigue, C. Warakulwit, J. Limtrakul, L. Bouffier, and A. Kuhn, Electrochim. Acta **56**, 10562 (2011).
[24] W. Liu, R. He, H. Zhu, H. Hu, M. Li, and X. Zhong Zhao, Appl. Phys. Lett. **96**, 053114 (2010).
[25] L. F. Valadares, Y.-G. Tao, N. S. Zacharia, V. Kitaev, F. Galembeck, R. Kapral, and G. A. Ozin, Small **6**, 565 (2010).
[26] S. Ebbens, M.-H. Tu, J. R. Howse, and R. Golestanian, Phys. Rev. E **85**, 020401 (2012).
[27] R. A. Pavlick, S. Sengupta, T. McFadden, H. Zhang, and A. Sen, Angew. Chem. **123**, 9546 (2011).
[28] W. Gao, M. D'Agostino, V. Garcia-Gradilla, J. Orozco, and J. Wang, Small **9**, 467 (2013).
[29] M. Khan, A. K. Sood, F. L. Deepak, and C. N. R. Rao, Nanotechnology **17**, S287 (2006).
[30] M. Feyen, E. Heim, F. Ludwig, and A. M. Schmidt, Chem. Mater. **20**, 2942 (2008).
[31] P. H. Jones, F. Palmisano, F. Bonaccorso, P. G. Gucciardi, G. Calogero, A. C. Ferrari, and O. M. Marago, ACS Nano **3**, 3077 (2009).
[32] R. Di Leonardo, A. Búzás, L. Kelemen, G. Vizsnyiczai, L. Oroszi, and P. Ormos, Phys. Rev. Lett. **109**, 034104 (2012).
[33] W. Wang, L. A. Castro, M. Hoyos, and T. E. Mallouk, ACS Nano **6**, 6122 (2012).
[34] S. Sundararajan, P. E. Lammert, A. W. Zudans, V. H. Crespi, and A. Sen, Nano Lett. **8**, 1271 (2008).
[35] J. Burdick, R. Laocharoensuk, P. M. Wheat, J. D. Posner, and J. Wang, J. Am. Chem. Soc. **130**, 8164 (2008).
[36] L. Baraban, M. Tasinkevych, M. N. Popescu, S. Sanchez, S. Dietrich, and O. G. Schmidt, Soft Matter **8**, 48 (2012).
[37] P. Calvo-Marzal, K. M. Manesh, D. Kagan, S. Balasubramanian, M. Cardona, G.-U. Flechsig, J. Posner, and J. Wang, Chem. Commun. 4509 (2009).
[38] S. Balasubramanian, D. Kagan, K. M. Manesh, P. Calvo-Marzal, G.-U. Flechsig, and J. Wang, Small **5**, 1569 (2009).
[39] T. R. Kline, W. F. Paxton, T. E. Mallouk, and A. Sen, Angew. Chem. Int. Ed. **44**, 744 (2005).
[40] A. Nourhani, P. E. Lammert, A. Borhan, and V. H. Crespi, Phys. Rev. E **87**, 050301(R) (2013).
[41] I. Sendiña-Nadal, S. Alonso, V. Pérez-Muñuzuri, M. Gómez-Gesteira, V. Pérez-Villar, L. Ramírez-Piscina, J. Casademunt, J. M. Sancho, and F. Sagués, Phys. Rev. Lett. **84**, 2734 (2000).
[42] S. Ebbens, R. A. L. Jones, A. J. Ryan, R. Golestanian, and J. R. Howse, Phys. Rev. E **82**, 015304 (2010).
[43] B. M. Friedrich and F. Jülicher, New J. Phys. **10**, 123025 (2008).
[44] N. A. Marine, P. M. Wheat, J. Ault, and J. D. Posner, Phys. Rev. E **87**, 052305 (2013).
[45] G. Dunderdale, S. Ebbens, P. Fairclough, and J. Howse, Langmuir **28**, 10997 (2012).
[46] P. E. Lammert, J. Prost, and R. Bruinsma, J. Theor. Biol. **178**, 387 (1996).
[47] R. Golestanian, T. B. Liverpool, and A. Ajdari, Phys. Rev. Lett. **94**, 220801 (2005).
[48] N. B. Saidulu and K. L. Sebastian, J. Chem. Phys. **128**, 074708 (2008).
[49] R. Golestanian, Phys. Rev. Lett. **102**, 188305 (2009).
[50] E. Yariv, Proc. R. Soc. A **467**, 1645 (2011).
[51] J. L. Moran, P. M. Wheat, and J. D. Posner, Phys. Rev. E **81**, 065302(R) (2010).
[52] J. G. Gibbs and Y.-P. Zhao, Appl. Phys. Lett. **94**, 163104 (2009).

[53] B. Sabass and U. Seifert, J. Chem. Phys. **136**, 214507 (2012).
[54] L. G. Leal, *Advanced Transport Phenomena: Fluid Mechanics and Convective Transport Processes* (Cambridge University Press, New York, 2007).
[55] S. Kim and S. J. Karrila, *Microhydrodynamics: Principles and Selected Applications* (Dover Publications, New York, 2005).
[56] R. Hsu and P. Ganatos, J. Fluid Mech. **207**, 29 (1989).
[57] S. Ye and R. L. Carroll, ACS Appl. Mater. Interfaces **2**, 616 (2010).
[58] Y. Wang, R. M. Hernandez, D. J. Bartlett, J. M. Bingham, T. R. Kline, A. Sen, and T. E. Mallouk, Langmuir **22**, 10451 (2006).